Computational Geosciences (2024) 28:341–354
https://doi.org/10.1007/s10596-023-10257-8

ORIGINAL PAPER

Implementation of Soreide and Whitson EoS in a GPU-based reservoir simulator

P. Panfili[1] · L. Patacchini[2] · A. Ferrari[1] · T. Garipov[2] · K. Esler[2] · A. Cominelli[1]

Received: 9 November 2022 / Accepted: 23 September 2023 / Published online: 21 October 2023

Abstract

Reservoir simulation is traditionally based on the assumption that water is an inert phase, while hydrocarbon components split into oil and gas phases. This approach is usually reasonable when modeling conventional hydrocarbon recovery, but specific applications may require accounting for mass exchange between the water and hydrocarbon phases. We here present the extension of our Graphics Processing Units (GPUs) compositional reservoir simulator (Esler et al. SPE J. **27**(01), 597–612, 2021) to support gas-water equilibrium. Specifically, the Søreide and Whitson equation of state (EoS) (Søreide and Whitson Fluid Phase Equilib. **77**, 217–240, 1992) was implemented to compute mutual solubilities of hydrocarbon/brine mixtures. The impact of salinity on phase equilibrium is accounted for, with salt being treated as an active tracer. The simulator uses a mass-variables formulation, meaning that little modifications to the construction of transport equations and Jacobian assembly was required; most of the required code changes are localized in the EoS module for the computation of component fugacities, and phase properties such as partial molar fractions and partial molar volumes. Treating salt as an active tracer instead of defining a further pseudo-component has an important advantage with the Søreide and Whitson EoS. If salinity changes as in water vaporization processes, our choice ensures that flash iterations can still be cast as a Gibbs Minimization problem with salinity being a constant parameter. On the contrary, salinity would change as flash iterations progress, jeopardizing the thermodynamic consistency of the phase equilibria. The overall reservoir simulation system of equations is still accurate to first order in time, at the cost of possibly slight volume imbalances at the end of converged timesteps. In this paper, we focused on CO_2 sequestration in saline aquifers, where solubility trapping is a key mechanism. The accuracy of our implementation with respect to conventional CPU ones is first demonstrated on a synthetic box model. We then select an open-access aquifer model (Gassnova 2016) to illustrate its applicability in an industrial setting. Finally, we show how being able to seamlessly run high resolution models allows for modeling of convective mixing. A key conclusion of this work is that the extreme performance of GPU-based reservoir simulation naturally transfers to new fields of study, which is critical when modeling saline aquifers whose extent is an order of magnitude larger than that of typical oil and gas fields.

Keywords GPU · CO2 sequestration · Phase equilibrium · Cubic EoS · Reservoir simulation

1 Introduction

Numerical simulation of gas injection into saline aquifers or into depleted hydrocarbon fields (whether for cyclic energy storage or for carbon capture) shares many aspects with the more established discipline of petroleum reservoir simulation. In particular, at the reservoir scale the fundamental equations are still first order mass conservation equations closed by the multi-phase extension of Darcy's law [3]. Provided a suitable relative permeability hysteresis model is used [16, 19], both structural and residual trapping can be modeled.

In the context of carbon capture, dissolution of CO_2 in the aqueous phase is also an important mechanism. Conventional compositional reservoir simulation however relies on cubic Equations of State (EoS) appropriate for hydrocarbon phases equilibrium [30, 36], while water is treated as a "dead" phase. Said EoS are not suitable to handle polar components such as H_2O.

A first approach to model hydrocarbon-water equilibrium in reservoir simulators is to retain a cubic EoS description of the hydrocarbon phases while computing the

✉ P. Panfili
paola.panfili@eni.com

Extended author information available on the last page of the article

hydrocarbon components' fugacities in the aqueous phase using Henry's constants, based on correlations fitted to experimental data [20]; this is the approach adopted by the GEM reservoir simulator [6]. A conceptually similar approach is to use gas dissolution tabulations vs. pressure (and possibly temperature and salinity) [5]. Such modeling is available, for example, in Nexus [15], ECLIPSE-300 with CO2SOL option [34], and Intersect [35]. Note that in these latter examples, the water component is not allowed to vaporize. The thermodynamic model of the TOUGH2 simulator [28] has gained wide acceptance for cases where H_2O and CO_2 are the only components (in addition to salts). For example, it is available in ECLIPSE-300 with CO2STORE option.

A second approach is to use more complex EoS suitable for hydrocarbon-water equilibrium (e.g., the cubic-plus-association EoS), but these are seldom used in reservoir simulation because of their computational cost [43]. A "practical" solution is to use asymmetric binary interaction coefficients (BICs), as proposed by [37], where specific temperature and salinity-dependent BICs are defined for the aqueous phase. This EoS, here referred to as the SW-EoS, is available in ECLIPSE-300 with GASWAT option, as well as in research codes such as MUFITS [1] and IHRRS [31]. It is also worth noting that similarly to the CO2SOL option, the GASSOL option in ECLIPSE-300 uses solubility tables, but possibly precomputed using the SW-EoS.

Finally, we observe that when H_2O and CO_2 are the only modeled components, the problem can be formulated in black-oil form by identifying H_2O with oil and CO_2 with gas. In this case, PVT properties can be either tabulated, or hard-coded within the simulator as in OPM-Flow [26].

Modeling CO_2 storage may require further physics in addition to the equilibrium of the aqueous and vapor phases, such as geochemical reactions for long term storage; these can be either modeled internally by the flow simulator [6], or simulated by explicit coupling of the flow simulator to a third party code [18, 39]. Coupled thermal and mechanical effects may also be important; notably, near-wellbore cooling due to the Joule-Thompson effect [25] can favor fracturing. Temperature also has an impact on pressure reached in the aquifer, which needs to be carefully predicted to study cap rock integrity [27].

CO_2 storage applications therefore require complex physics, and possibly very large grid models [41]. The latter requirement is due to the potentially large extent of saline aquifers, as well as to the need for fine resolution in regions where CO_2 displaces water or undergoes convective mixing. This requirement is particularly significant for industrial or general-purpose simulators using first order in space and time numerical schemes, while more specialized codes designed to study specific phenomena benefit from higher order methods [23].

A possible avenue to deliver a high-performance industrial-grade simulator able to tackle new applications such as CO_2 storage is to start from scratch with a design for modern hardware; this is the approach chosen for GEOSEX [14]. Alternatively, one may progressively incorporate the necessary modeling features into an existing high-performance code. An example is Intersect, which was initially developed for both isothermal and thermal petroleum recovery applications, and was later enriched with three-phase equilibrium capabilities and support for geochemical reactions. A similar approach of extending our industrial GPU-based simulator [9, 38] is here chosen.

The end goal is to support a full three-phase model, which can also be used for modeling CO_2 EOR or CO_2 storage in retrograde condensate fields, using the Søreide and Whitson EoS approach. In this work we limit ourselves to two-phase reservoir conditions, namely aqueous-vapor, which allows us to reuse existing stability and flash routines [11]. Nevertheless, the full implementation has been designed as being three-phase, i.e., there is no replacement of oil by water behind the scenes.

The paper is structured as follows. We start by describing the selected numerical formulation and physical modeling approach, and demonstrate the computational efficiency of the implementation using a methodology inspired by [9]. We then select an open-access aquifer model used for CO_2 sequestration studies [8] to validate the accuracy of the model in an industrial setting. Finally, we show how being able to seamlessly run high resolution models allows for observation of convective mixing.

2 Overview of simulator modifications

A detailed description of our compositional simulator can be found in [9] for the usual case where hydrocarbon components can partition between oil and gas phases, while water is a dead phase; we liberally refer to any non-water component as a hydrocarbon.

Before discussing the numerical formulation and the physical models used in the code, it is useful to consider the flow-chart of the GPU simulator timestepping in Fig. 1, after [24].

The different steps in Fig. 1 are described as follows, with a highlight of noteworthy changes performed in this work.

1. At the beginning of each timestep, well potentials are evaluated to compute guide-rates needed for rule-based allocation.
2. All relevant cell properties are computed, including fluid (density, viscosity, partial molar fractions, ...) and rock-fluid (relative permeabilities and capillary pressures).

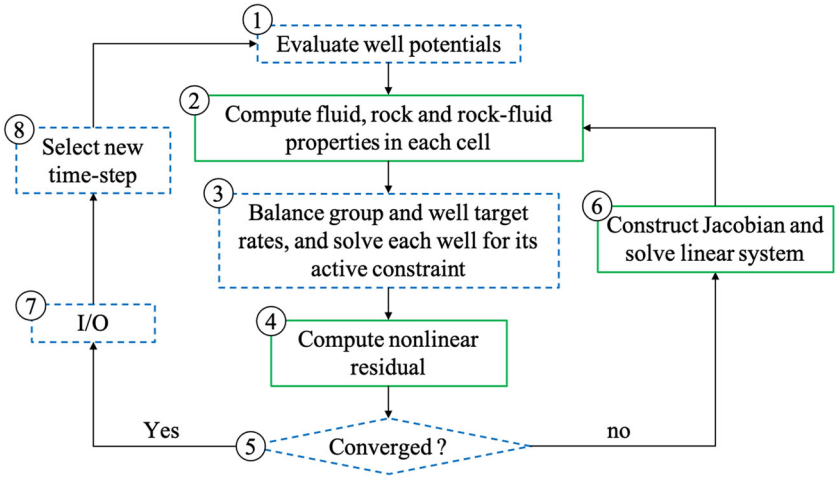

Fig. 1 Simplified flowchart of a reservoir simulation timestep. Solid green and dashed blue boxes indicate operations performed on the GPU and CPU, respectively. After [24]

Noteworthy modifications: Phase equilibrium calculations use the SW-EoS, possibly function of salinity, and water-phase properties (density / viscosity) use specific correlations.

3. Well groups are balanced at frozen reservoir conditions.
4. The reservoir-well system of equations' residual is computed. *Noteworthy modifications*: The system of equations used to compute the residual accounts for hydrocarbon and water components transport in both the aqueous and vapor phases.
5. The residual is used (possibly in conjunction with variables change criteria) to decide on convergence.
6. If the timestep is unconverged, the simulator constructs the Jacobian system and solves the corresponding linear system of equations to proceed to the next Newton iteration. *Noteworthy modifications*: The Jacobian is constructed according to the set of equations described in item 4.
7. If the timestep is converged, the simulator performs required I/O tasks.
8. Selects a new timestep length and proceeds to a new timestep.

3 Formulation

3.1 Governing equations

In this work, we allow hydrocarbon and water components to be in thermodynamic equilibrium, but limit ourselves to cases without liquid oil at reservoir conditions (see Fig. 2-left). The reservoir physics is therefore governed by the following n_c conservation equations:

$$\frac{\partial}{\partial t}\left[\phi\left(w_i b_w S_w + y_i b_g S_g\right)\right] + \nabla\cdot\left(w_i b_w \mathbf{u}_w + y_i b_g \mathbf{u}_g\right) + q_i = 0\,,\ \forall\, i \in [1, n_c]\,, \quad (1)$$

where S_φ, $\mathbf{u}_\varphi$ and b_φ are the saturation, Darcy velocity and molar density of phase φ, respectively, and $\underline{w}$ and $\underline{y}$ are the molar fraction arrays in the water and gas phases; q_i is a source-term density for component i, arising, for example, from producer or injector wells.

The conservation equations are closed by the multiphase extension of Darcy's law [3]:

$$\mathbf{u}_\varphi = -\mathbf{K}\cdot\frac{k_{r\varphi}}{\mu_\varphi}\left(\nabla p_\varphi - \rho_\varphi \mathbf{g}\right)\ ,\ \forall\varphi \in \{g, w\}\ , \quad (2)$$

where $\mu_\varphi, \rho_\varphi, k_{r\varphi}$ and p_φ are the viscosity, mass density, relative permeability and pressure of phase φ, respectively. $\mathbf{K}$ is the permeability tensor and $\mathbf{g}$ is the gravitational acceleration vector.

The aqueous and vapor phases are assumed to be in instantaneous thermodynamic equilibrium, with n_c equilibrium constraints [22], defined as:

$$f_{i,w}\left(p_g, \underline{w}\right) - f_{i,g}\left(p_g, \underline{y}\right) = 0\ ,\ \forall i \in [1, n_c]\ , \quad (3)$$

where $f_{i,\varphi}$ is the fugacity of component i in phase φ. In Eq. 3, we neglect the pressure difference between phases and evaluate the fugacities at the gas pressure p_g.

3.2 Discretization

The simulator uses a mass-variables formulation with an extended set of $n_c + 3$ primary variables per gridblock; these are the hydrocarbon volume-weighted pressure p_h (equal to p_g in the absence of oil phase), water and gas saturations S_w and S_g, and the mole numbers N_i, $i \in [1, n_c]$. This is slightly different from other mass-variables formulations [15, 34] that arrive at phase saturations (to be used in the extended Darcy's law) by back-calculation from mole numbers and pressure.

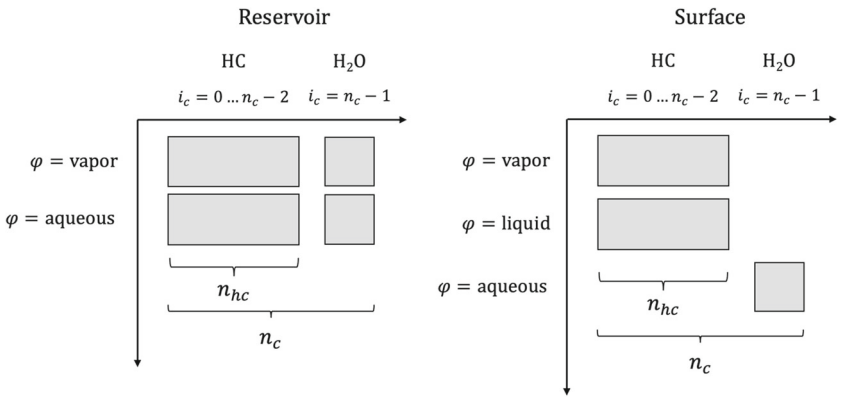

Fig. 2 Component-phase repartition diagrams for reservoir and surface condition fluids. While hydrocarbons and water can be in thermodynamic equilibrium at reservoir conditions, we consider the water phase to be dead at surface conditions

Relaxing the dead water phase assumption of the original implementation [9] requires code modifications which we can broadly separate in two categories.

- Generalize the volume balance and mass conservation equations to account for the transport of hydrocarbon components in the water phase and water component in the hydrocarbon phases.
- Generalize the calculation of partial molar fractions and partial molar volumes for the multiple combinations of two-phase cases (gas-water, gas-oil, oil-water) and the three-phase case, and develop a three-phase flash.

The results presented in this paper are limited to cases without liquid oil at reservoir conditions, hence calculation of three-phase partial molar fractions and volumes as well as three-phase equilibrium are not required.

Using a first-order upstream mobility weighting, time integration between t^n and t^{n+1} of the conservation equations yields the following mass balance residual (MBR):

$$\mathrm{MBR}_{i;\ell} = \frac{N_{i;\ell}^{n+1} - N_{i;\ell}^{n}}{\Delta t^n} + \sum_{\ell' \in \mathscr{C}(\ell)} T_{\ell,\ell'} \cdot [(w_i \lambda_w)_{\uparrow} \Delta\Phi_{w;\ell,\ell'} + (y_i \lambda_g)_{\uparrow} \Delta\Phi_{g;\ell,\ell'}] + Q_{i;\ell}, \ \forall i \in [1, n_c], \quad (4)$$

where $\Delta t^n = t^{n+1} - t^n$ is the timestep length, $\mathscr{C}(\ell)$ is the set of cells connected to cell ℓ, $T_{\ell,\ell'}$ is the transmissibility between cells ℓ and ℓ', and "$\uparrow$" indicates the upstream cell for the phase at hand. Only a two-point flux approximation (TPFA) is considered at the moment.

In Eq. 4 we also defined the mobility of phase φ as $\lambda_\varphi = k_{r\varphi}/\mu_\varphi$, and the potential difference between two grid blocks ℓ and ℓ' as $\Delta\Phi_{\varphi\,\ell\to\ell'} = p_{\varphi,\ell} - p_{\varphi,\ell'} - \rho_{\varphi,\ell,\ell'}\, g \Delta d_{\ell\to\ell'}$, where $\Delta d_{\ell\to\ell'}$ is their depth difference, and $\rho_{\varphi,\ell,\ell'}$ is the mass density of phase φ at reservoir conditions at their interface.

In addition to Eq. 4, we include equations for the gas and water phase volume balance residuals (VBRs),

$$\mathrm{VBR}_{\varphi;\ell} = \mathrm{PV}_\ell\left(p_g\right) S_\varphi - V_\varphi\left(p_g, \underline{N}_\ell\right), \quad \forall \varphi \in \{g, w\}, \quad (5)$$

where PV_ℓ is the pore volume of cell ℓ (a function of pressure in presence of rock compressibility), and V_φ is the volume of phase φ computed using compositions obtained by the phase equilibrium calculations.

The three time discretization schemes described in [9] can be used in combination with the extensions described here: the fully implicit method (FIM); the implicit pressure, explicit mobility method (IMPEM); and the adaptive implicit method (AIM).

Although the code supports any number of components, the examples presented in this paper only contain H_2O and CO_2. For such a small component-set, there is close to no penalty for using FIM over AIM, hence FIM will be used.

3.3 Well and separator modeling

We utilize bottom-hole pressure as a single variable defining the well state, and compute the hydrostatic head by integrating the density along the wellbore based on explicit inflows. The fluid description in the wellbore follows that of the reservoir, i.e., in this work only supports an aqueous and vapor phase (see Fig. 2-left).

Well and group controls are often based on surface volumetric rates and the same thermodynamic model needs not be used. In this work, we choose to keep the usual liquid-vapor equilibrium with a dead aqueous phase at surface conditions (see Fig. 2-right). We consider an idealized separation process depicted Fig. 3 where the production stream is first dehydrated, before passing through a familiar multi-stage separator where each stage is modeled by either an EoS or a gas-plant table.

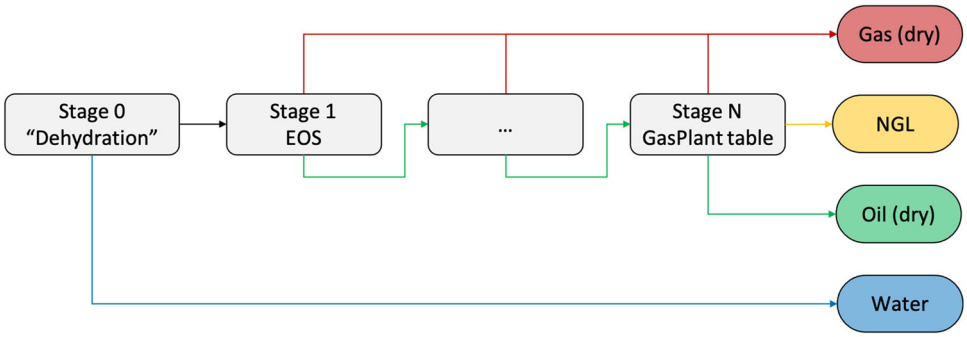

Fig. 3 Idealized separator process considered in this work. The water component is extracted first, while the hydrocarbon stream is separated following a conventional multi-stage process. Each stage can be modeled with an EoS or a gas plant table

We recognize that in reality dehydration may happen later, and disregarding the water component during the separation process may impact the vapor-liquid equilibrium. Our approach nevertheless has the advantage of simplifying the work required for extending a conventional reservoir model to support three-phase equilibrium.

4 Physical models

4.1 Rock and rock-fluid models

The same rock and rock-fluid models as in conventional reservoir simulations are considered. Because here only gas and water phases are present at reservoir conditions, $p_{cgw} = p_g - p_w$, k_{rg} and k_{rw} are function of S_g; also, gas is naturally the non-wetting phase in relative permeability hysteresis modeling. Porosity is considered to be a function of pressure according to a constant pore compressibility or rock compaction tables.

4.2 Salt-free compositional description

We follow a salt-free compositional description, meaning that the molar composition array $\underline{N}$ or the aqueous phase composition array $\underline{w}$ do not include salts or other additives. The water component is therefore pure H_2O with $\mathrm{MW}_{H_2O} = 18.015$ g/g-mol, and the salt concentration C_S is a parameter in phase equilibrium and phase property calculations.

Salinity is at the moment treated as an active tracer, i.e. it is updated at the end of each converged time-step. The salt-free approach could, nevertheless, also be used if salt were treated monolithically with the main components.

In conventional reservoir simulators, C_S is often expressed in kg/sm^3 or lb/stb (mass of salt per standard volume of brine, i.e, water plus salt) for control and reporting purposes. However, phase equilibrium models are often based on molality m_s, expressed in g-mol/kg (gram-mole of salt per kilogram of H_2O).

The number of water moles can be obtained from surface brine volume V_w^{stc} and C_S as

$$N_{H_2O} = V_w^{\mathrm{stc}} \cdot \frac{\rho_w^{\mathrm{stc}} - C_S}{MW_{H_2O}}, \tag{6}$$

where ρ_w^{stc} is mass density of brine at surface conditions; the molality m_s can be obtained as

$$m_s = 1000 \frac{C_S}{MW_{salt}\left(\rho_w^{\mathrm{stc}} - C_S\right)}. \tag{7}$$

4.3 Phase equilibrium

A phase equilibrium model is essentially needed for two different operations.

- To compute the split of a feed in multiple phases, along with the composition of said phases (flash calculation).
- To compute the partial molar fractions of a multiphase mixture previously equilibrated with a flash, which we define as how the number of moles of a specific component in a specific phase varies when the feed amount of said component varies.

Both operations need to be computed on a per-cell basis at each nonlinear iteration (step 2 in Fig. 1). Each cell being independent of each other, this procedure exhibits a high degree of parallelism and is well suited for GPUs. The flash procedure itself being iterative and each cell requiring a different number of iterations, a possible way to improve GPU occupancy is to group cells in batches having a similar number of expected iterations. We use one thread per cell for fixed-point iterations (first-order flash iterations), and one thread per component for operations requiring matrix inversion (second-order flash iterations, and partial molar fraction calculations), as discussed by [11].

Both operations also need to be computed on a per-well basis at each nonlinear iteration (step 3 in Fig. 1). In this case, parallelism is not sufficient to warrant GPU execution, hence well solves are handled by the CPU cores.

Fugacities needed for the thermodynamic equilibrium constraints Eq. 3, are obtained via the SW-EoS [37], an extension of the PR-EoS with two main modifications. First, the water attraction parameter is modified as

$$\alpha_{H_2O} = 1 + 0.453 \cdot \left[1 - \left(1 - 0.0103 m_s^{1.1}\right) T_{rH_2O}\right] + 0.0034 \cdot \left(T_{rH_2O}^{-3} - 1\right) , \quad (8)$$

where T_{rH_2O} is the reduced water temperature, and m_s is the NaCl molality (no other salts are considered). Second, the binary interaction coefficients between hydrocarbons or other light gases (CO_2, H_2S and N_2) and water in the aqueous phase are expressed as a function of their reduced temperatures and m_s. In this paper, benchmark cases contain CO_2 only, and the original correlation published by [37] is used:

$$k^{aq}_{CO_2,H_2O} = -0.31092 \left(1 + 0.15587 m_s^{0.7505}\right) + 0.2358 \left(1 + 0.17837 m_s^{0.979}\right) T_{rCO_2} - 21.2566 \exp\left(-6.7222 T_{rCO_2} - m_s\right) . \quad (9)$$

There have since been alternative expressions proposed for the CO_2-water BICs, such as the one of Yan et al. [42], used for example in IHRRS [31]. Correlations for additional components such as H_2 have also been proposed by [4]. A summary of correlations for BICs between dissolved components in the aqueous phase and water to be used with SW-EoS can be found in [1].

It is worth noting that flash calculations for gas-water systems (i.e., no oil) are not challenging. Typical reservoir or aquifer temperatures are too low for the mixture to approach critical conditions, hence the vapor phase is mostly comprised of hydrocarbons and the aqueous phase is mostly comprised of water component. This fortunate situation will change when we extend the code to support a full three-phase equilibrium (i.e., gas, oil and water at reservoir conditions), as the number of phase boundaries increases, in addition to the hydrocarbon phases possibly approaching their critical point.

4.4 Phase properties

The water phase density at reservoir conditions is given, in the absence of hydrocarbon dissolution, by:

$$\rho_{w0}(p, C_S) = \frac{\rho_w^{stc}(C_S)}{B_w(p, C_S)} , \quad (10)$$

where ρ_w^{stc} is the surface mass density of brine and B_w is its formation volume factor. These can either be tabulated vs. salinity and reservoir pressure, or computed with a built-in correlation that we take from [40].

The impact of hydrocarbon dissolution on water phase density is accounted for using Ezrokhi's correction as

$$\log_{10}\left(\frac{\rho_w}{\rho_{w0}}\right) = \sum_{i \in [1..n_h]} \xi_i \bar{w}_i , \quad (11)$$

where the ξ parameters are taken as a function of temperature, and $\bar{w}_i$ is the mass concentration of component i in the aqueous phase. For CO_2, we use the parameters from [2].

Similarly, the water phase viscosity in the absence of hydrocarbon dissolution, μ_{w0}, is either tabulated or computed with a built-in correlation, and its changes due to hydrocarbon dissolution are accounted for using Ezrokhi's correction as

$$\log_{10}\left(\frac{\mu_w}{\mu_{w0}}\right) = \sum_{i \in [1..n_h]} \chi_i \bar{w}_i , \quad (12)$$

where the χ parameters are taken as a function of temperature.

The gas phase density is computed from the EoS, while its viscosity is calculated using either the Lohrentz-Bray-Clark [21] or the Pedersen [29] correlations.

5 Model #1: tiled box model - scaling experiments

5.1 Elementary tile

We start with an investigation of the computational performance scaling with model size. For this purpose, we extend the fifth comparative solution project grid [17] to obtain a simple box model of dimensions $82 \times 45 \times 30$ cells whose properties are given in Table 1.

Gas and water relative permeability and capillary pressure curves are taken from the Smeaheia dataset [8], as shown in Fig. 4.

The initial datum pressure and temperature are 1191 psi and 98.6°F, respectively. The model is initialized with water only, can host two components (CO_2 and H_2O), and contains one CO_2 injector and one producer. The injector is controlled by surface CO_2 rate (40 MMscf/day) and the producer by surface water rate (18 Mstb/day). The injector is perforated

Table 1 Static properties of an elementary tile used for the scaling test

Layers	$k_x = k_y$ (mD)	k_z (mD)	ϕ	$\Delta x = \Delta y$ (ft)	Δz (ft)
1-10	500	50	0.3	500	20
11-20	50	50	0.3	500	30
21-30	200	25	0.3	500	50

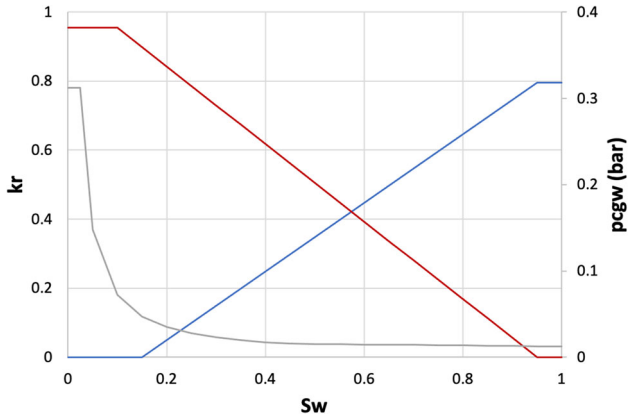

Fig. 4 Relative permeability and capillary pressure curves of the Smeaheia dataset (k_{rg} in red, k_{rw} in blue, and p_{cgw} in dashed purple)

in cells ($i = 61$, $j = 23$, $k = [1, 10]$), and the producer in cells ($i = 21$, $j = 23$ and $k = [20, 30]$); both have a wellbore diameter of 0.5ft.

The simulation duration (300 years) is chosen such that CO_2 breaks through toward the end. Figure 5 shows a 3D view of the elementary tile at the end of the simulation.

5.2 Results benchmark against the reference solution

We start by benchmarking our simulator (hereafter referred to as "GPU simulator") against `ECLIPSE-300` with GASWAT option (hereafter referred to as "Reference simulator").

The reference simulator considers water and hydrocarbons to be at equilibrium at surface conditions, while we use the separator concept of Fig. 3 where gas is dried. It is therefore important to add a custom gas-plant table to the separator of the reference model to force separation of H_2O and CO_2.

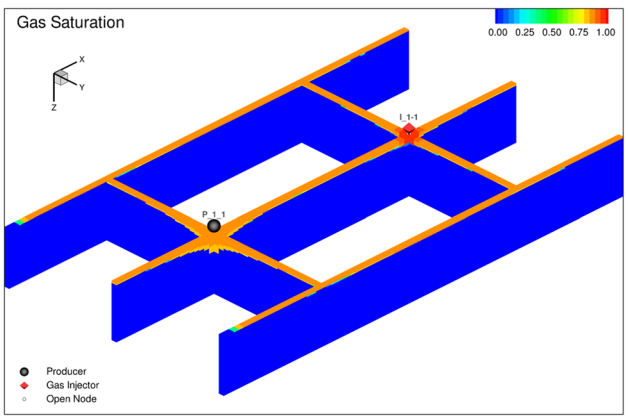

Fig. 5 "Waffle" view of an elementary tile used for the scaling test, colored according to the CO_2-rich phase (labeled as gas) saturation at the end of the simulation (year 300)

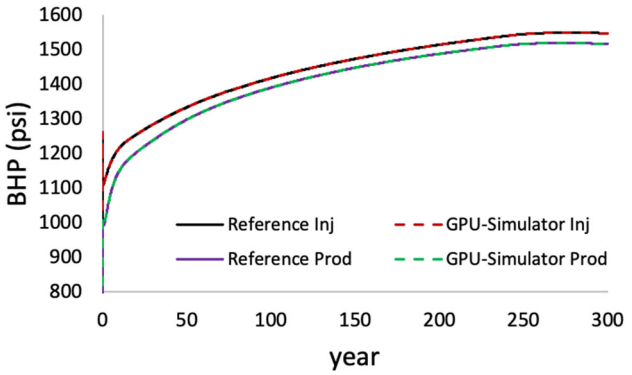

Fig. 6 Comparison of the injector and producer bottom-hole pressure profiles for an elementary tile, as computed by the GPU simulator and the reference simulator

Figure 6 shows a comparison of injector and producer bottom-hole pressure profiles; the agreement is excellent, validating the implementation of both phase equilibrium and phase properties evaluations.

5.3 Weak and strong scalability

To measure throughput vs. model size, we tile the model repeatedly in both horizontal directions, mirroring adjacent copies, so that by symmetry, each well in the resulting tiled models injects or produces precisely as in the original, untiled model. We may then investigate how the runtime varies with model size while keeping the nonlinear behavior the model essentially fixed. In order to increase performance and make it possible to simulate larger models, the simulator can take advantage of multiple GPUs, either inside a single node or distributed across multiple nodes. In order to explore the efficiency of multi-GPU simulation, we record runtimes on one, two, and four GPUs for a range of tiled models up to about 25M cells. We then plot the resulting simulation throughput, defined as the number of active cells divided by simulation elapsed time in seconds in Fig. 7. Note that because of memory limitations, the single GPU simulations have a maximum model size which is about 1/4 of the four GPU simulations and likewise for the two GPU simulations. Also, note that since the geometry is extremely simplified, the absolute throughput shown here should not be considered representative of a more complex model derived from a realistic geomodel.

As discussed by [9], the efficiency of a GPU-based simulators is maximized when abundant parallelism is exposed in the form of large models. Therefore, as the model size is increased, the overall simulation throughput increases until all GPU resources are fully utilized and performance saturates. For multi-GPU simulations, the model size at which performance saturates grows roughly linearly with the number of GPUs, since the simulation cells are distributed equally

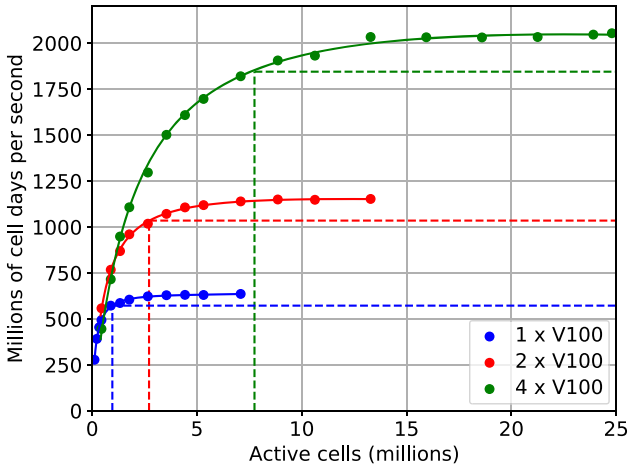

Fig. 7 Simulation throughput as a function of model size on 1, 2, and 4 NVIDIA Tesla V100 GPUs. The dashed lines show the vertical and horizontal positions at which each fit curve reaches 90% of its maximum

across the GPUs. In Fig. 7, it can be seen that for the case of this two-component model, between 1.0M and 1.9M cells are needed for the throughput to reach 90% of its maximum. Alternatively, multiple model realizations may be run simultaneously on a single GPU to reach a very similar maximum throughput even for very small models [12].

The growth in performance with increasing processor count is usually discussed in terms of *weak* and *strong* scalability. Weak scalability is a measure of the relative cost of simulations as the number of processors is increased in proportion to the model size. In an ideal system with perfect preconditioners, zero communication latency, and infinite communication bandwidth between processors, we would expect to observe constant runtime if the model size is increased in proportion to the number of GPUs. In reality, however, multi-GPU runs incur overhead due to the communication required between GPUs and perfect weak scalablility is not expected. In this example, we see that in moving from one to four GPUs, overall throughput increases by a factor of over 3.2, corresponding to a weak scalability of approximately 80%.

Strong scalability is a measure of how performance on a fixed model changes as the numbers processors is raised. The simulator's strong scalability on this synthetic model problem can be assessed by considering the intersection of the 1, 2, and 4-GPU performance curves with a vertical line. From the figure, we can see that in going from 1 to 2 GPUs, the performance increases by a factor of 1.8, while in going from 2 to 4 GPUs, the performance increases by a more modest factor of 1.6. In evaluating this scalability, one should bear in mind that each V100 GPU contains 5120 cores operating in parallel, so that the strong scalability in moving from one to two GPUs is lower than may be expected in moving from one to two CPU cores.

6 Model #2: Smeaheia - large scale CO_2 sequestration in a deep aquifer

6.1 Aquifer and model background

We here consider a CO_2 sequestration problem based on the Smeaheia case [33], a publicly available data-set [8] developed to assess the carbon storage potential in the homonymous area of the Norwegian continental shelf [13].

The Smeaheia area is located in the Stord Basin, 50 km off shore the coast of Norway near Bergen. A set of faults separates it from the Troll Field in the West and the Caledonian Basement Complex toward the East [10]. The public data-set has 1.5 million active cells (106x174x100 corner-point grid) with five producers (one horizontal and four vertical) to mimic pressure depletion deriving from the nearby Troll field, and one gas injector. It has a black-oil formulation, whereby water is formally treated as oil, and CO_2 as gas, which allows running the model with a conventional simulator; dry gas is considered [i.e., water (formally oil)] cannot vaporize. Injection starts after 31 years of depletion with a constant CO_2 injection rate of 5.9 MSm^3/d and continues for 25 years; simulation is then continued for additional 253 years to monitor CO_2 plume migration. Figure 8 shows a 3D view of the model colored by porosity.

The GPU simulator can directly run the black-oil model, as well as run a corresponding compositional model in which aqueous-vapor equilibrium is described using the Søreide and Whitson EoS, with CO_2 and H_2O components, and using a reservoir temperature of 37°C.

6.2 Results benchmark with the reference solution, in compositional mode

Figures 9 and 10 show the gas saturation and the CO_2 aqueous molar fraction, respectively, after ten years of injection in a region of layer 80 close to the injector. In the bottom part of Fig. 10 results are filtered considering only saturated cells; as expected the CO_2 molar fraction is approximately constant there (according to the Gibbs phase rule, the composition of two phases in equilibrium in the presence of two components only depends on pressure and temperature, but not on the feed). Saturation maps obtained with the reference and the GPU compositional simulators show excellent visual agreement.

6.3 Impact of CO_2 solubility in water and comparison with black-oil runs

Figure 11 compares the gas saturation map at year 2192 in the top layer of the model for four different fluid models; all cases have been run with the GPU simulator.

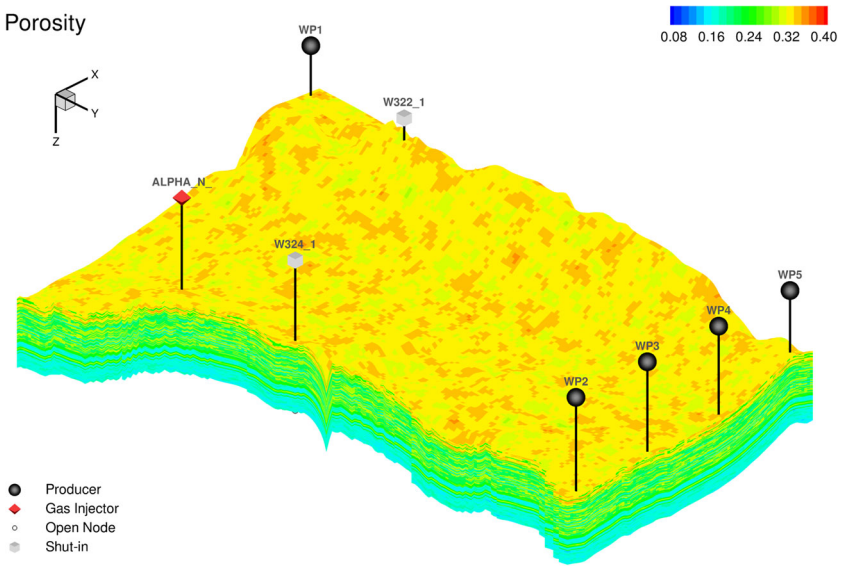

Fig. 8 3D view of the Smeaheia model [8] colored by porosity; "ALPHA_N" is the CO_2 injector

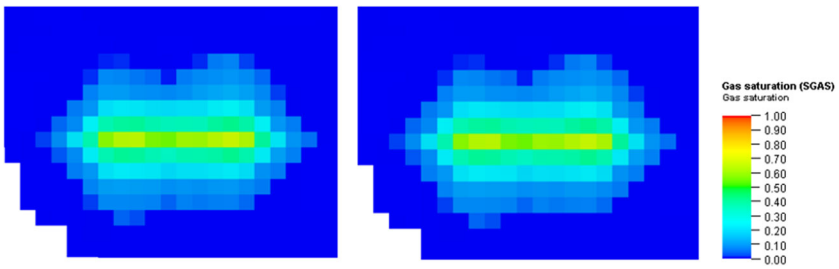

Fig. 9 Gas saturation in layer 80 after ten years of injection computed by the reference (left) and the GPU reservoir simulator (right)

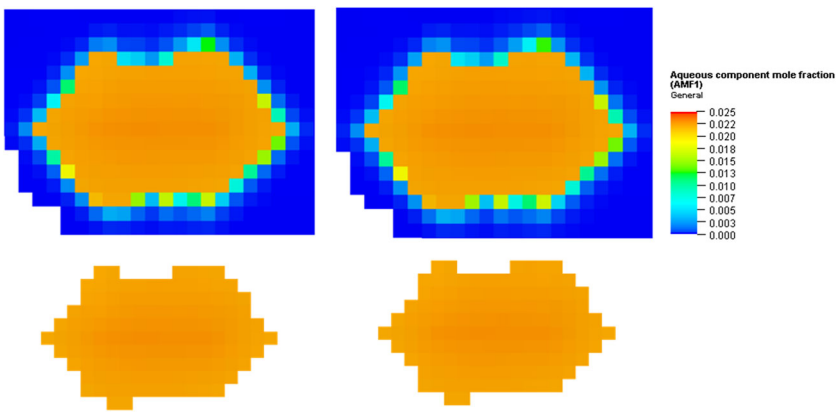

Fig. 10 CO_2 aqueous molar fraction in layer 80 after ten years of injection computed by the reference (left) and the GPU reservoir simulator (right). The bottom color-plots only show saturated cells, where the aqueous-phase composition is almost constant

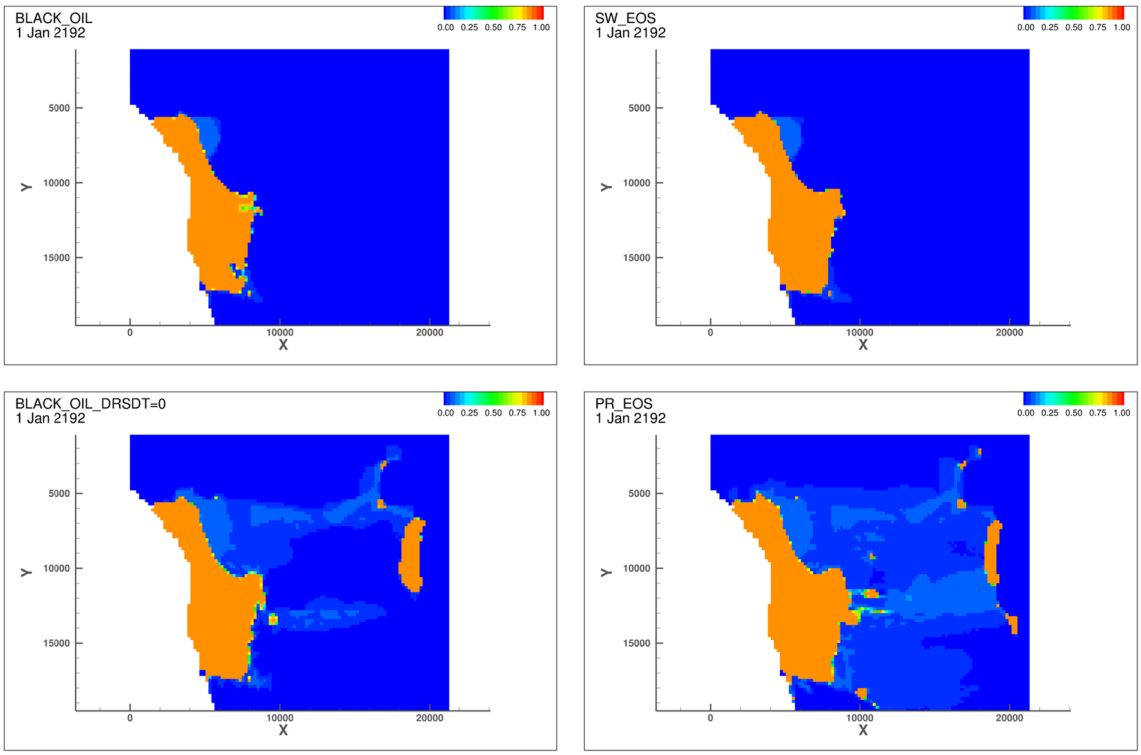

Fig. 11 Comparison of gas saturation maps at year 2192 in the top layer of the model, obtained with the GPU simulator with four different fluid models. Top-left: black-oil model; top-right: compositional model with SW-EoS; bottom-left: black-oil model without gas dissolution (DRSDT=0); bottom-right: compositional model with classic PR-EoS where hydrocarbons cannot dissolve in the aqueous phase

It can be seen that there is a good qualitative agreement between the black-oil and the compositional maps. The slight discrepancies are due to the fact that the black-oil tables from [8] have been generated from a model that is different from the combination of SW-EoS and Ezrokhi's modifiers, and partially due to the fact that water vaporization is neglected in the black-oil case (note that it could have been included with a generalized black-oil approach).

There is also a good qualitative agreement between the black-oil and the compositional maps when CO_2 dissolution in the aqueous phase is prevented. In this case, we see that the gas migrates from the injection structure to a secondary structure in the east; this clearly shows the importance of proper CO_2 solution modeling.

The average reservoir pore-volume weighted pressure is reported in Fig. 12. As expected, the pressure build up is

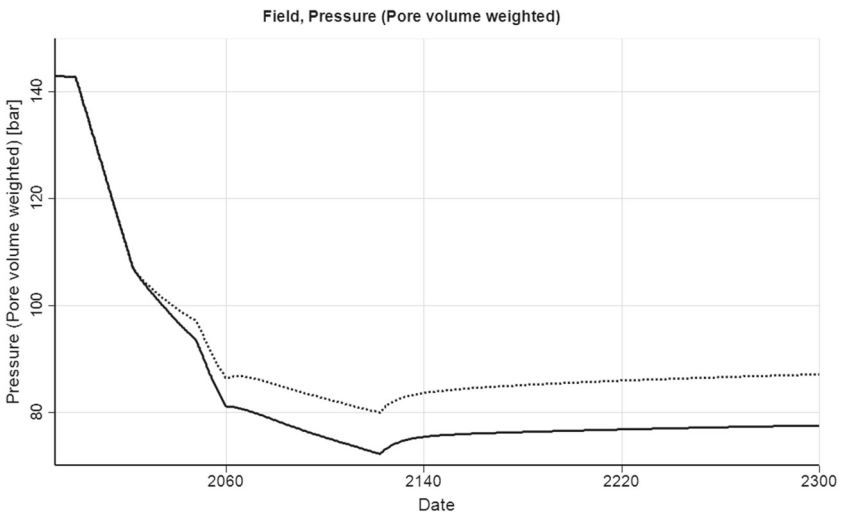

Fig. 12 Average pore pressure versus time for the cases with (solid line) and without (dotted line) CO_2 solubility in water

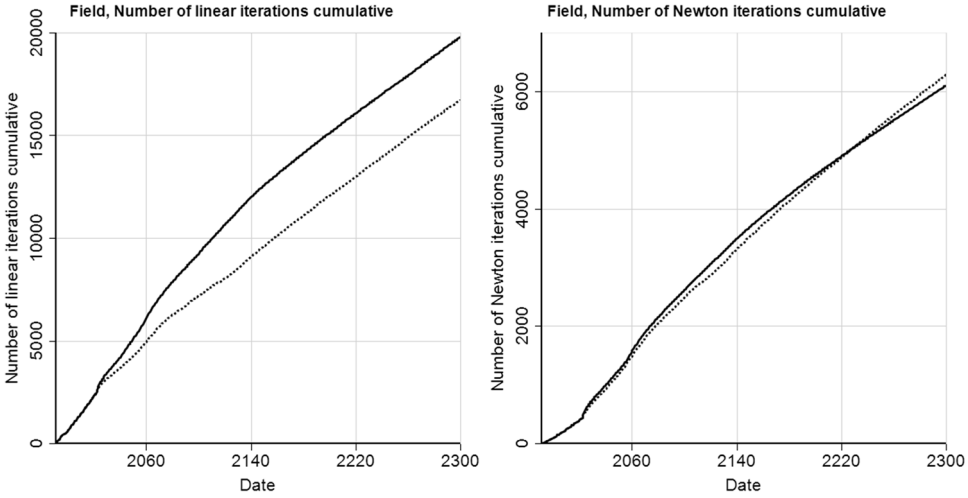

Fig. 13 Computational performance comparison for the case with (dotted) and without (solid) CO_2 solubility in water. Cumulative number of linear iterations (left) and cumulative number of Newton (right)

higher for the dead water case due to the fact that all CO_2 remains in the vapor phase; in the gas-water equilibrium case, approximately 40 Mton of the total 100 Mton of stored CO_2 is trapped in solution.

It is important to note that the results presented above are used to illustrate the impact of aqueous-vapor equilibrium, and do not represent a case study. In particular, relative permeability and capillary pressure hysteresis, which would be responsible for residual trapping, are not accounted for.

6.4 Computational performance

Figure 13 shows the cumulative number of Newton and linear iterations for the two compositional runs (with and without aqueous-vapor equilibrium) performed with the GPU simulator; default convergence criteria and a maximum timestep of 50 days are used (note that timesteps of one year would still allow convergence). Both runs take a similar number of Newton iterations, while the simulation including aqueous-vapor equilibrium takes slightly more linear iterations. This is likely explained by the fact that the system stiffness is increased by the thermodynamic coupling between phases, although it could also be due to the different physical evolution of the system over time.

In this model, the cost of EoS equilibrium calculations is in the order of 3%, i.e., close to negligible. The slightly higher number of linear iterations in the run with equilibrium causes a slight increase in runtime, from ∼2,000s to ∼2,400s on a single V100 GPU. Notably, the computational overhead is even less if we use 4 V100 GPUs instead of 1; in that case the simulation accounting for gas solubility is only 8% slower.

Another worthy performance metric is the ratio of black-oil vs. corresponding compositional run. When accounting for equilibrium, the black-oil run takes ∼1,500s, meaning that the compositional simulation runs in approximately 1.6x the time of its black-oil counterpart. This is aligned with what was observed in [9] for conventional models with two hydrocarbon components in equilibrium and dead water.

7 Model #3: Gravity-driven fingering effects

Among the various mechanisms involved in CO_2 sequestration, the approach described in this work enables accounting for solution trapping of CO_2 in resident water. During injection, CO_2 will start accumulating below the caprock due to gravity forces, and progressively begin to dissolve in the water located at the top of the underlying aquifer. CO_2 saturated water becomes denser than initial resident water and starts to sink down initiating unstable viscous fingers.

The triggering of fingers is governed by the interplay between gravity forces and physical diffusion. Numerical modeling of gravity-driven fingers for research purposes is typically performed with high order numerical schemes to limit numerical dispersion which may, otherwise, overshadow physical diffusion [7, 23, 32].

Table 2 Water properties

$\rho_{w,surf}$ (Kg/m^3)	B_w	c_w (1/bar)	μ_w (cP)
1002	1	$5.9 \cdot 10^{-5}$	0.655

Table 3 Ezrokhi's coefficients for CO_2 [2]

C_0	C_1	C_2
0.1033	$-2.3 \cdot 10^{-5}$	$-2.0 \cdot 10^{-6}$

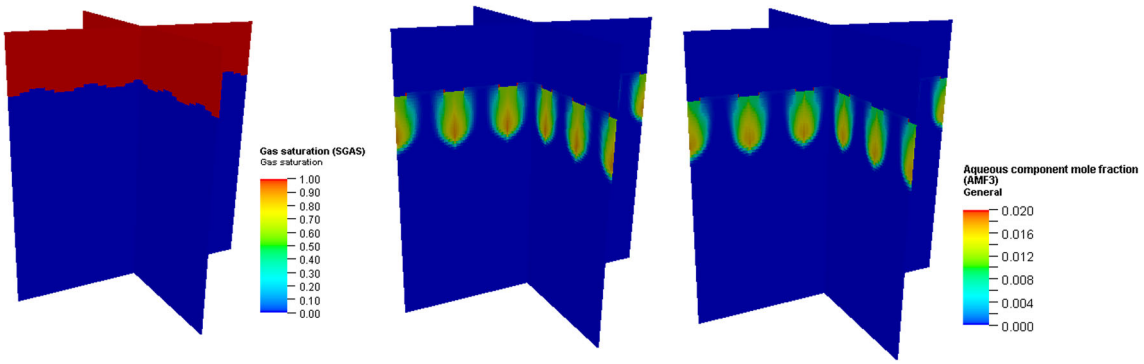

Fig. 14 Initial fluid distribution (left) and CO_2 aqueous molar fraction in two cross sections after 680 years of simulation for of the 4-million cell model (middle) and the 16-million cell model (right)

The GPU simulator currently does not support diffusion, hence any initial perturbation of the interface between CO_2-saturated brine and resident water would trigger an instability, whose long-term behavior would be governed by numerical dispersion. Provided the fingers are not expected to saturate within the reservoir thickness however, the ability to model the resulting convective mixing in a conventional, low order simulator without diffusion is still of interest; this may require very refined grids.

As a representative example, we considered a 200x200x100 grid (4 million active cells) with cell size equal to 5m x 5m x 10m, a horizontal permeability of 100 mD, a vertical permeability of 10 mD and porosity equal to 10%. The reservoir temperature is constant and equal to 40 °C. The initial pressure is set equal to 350 bar. The upper part of the model is fully saturated with CO_2, while the lower part with H_2O. A variable saturation perturbation is introduced at the contact in order to trigger the instabilities. We have arbitrarily selected a wavelength equal to 1/5 of the domain width. Water properties are reported in Table 2, while Ezrokhi's coefficients for CO_2 are reported in Table 3. Rock compressibility is set equal to $5 \cdot 10^{-5}$ 1/bar.

With the GPU simulator, it is easily possible to further refine the original model; here, we tested a 400x400x100 grid resulting in a total of 16 million active cells. The simulation runtime using 4 V100 GPUs was 15 min for the 4-million cell model and 73 min for the 16-million cell model. A maximum time-step length of 100 days was used in both cases.

Figure 14 shows the CO_2 fraction in the aqueous phase after 680 years of simulation for the base and the refined cases. The differences in terms of results for the two cases are negligible.

At the initial interface between gas phase and (pure) water phase, gravity forces work to flatten the contact: this triggers counter-current flow and the dissolution of CO_2 into pure water. As inter-phase mass exchange around the contact progressively reduces, water with the highest concentration of dissolved CO_2 migrates towards the bottom of the fingers.

8 Conclusions and way forward

A GPU-based compositional simulator, originally conceived to tackle typical petroleum-related problems, has been extended to support hydrocarbon-water equilibrium, necessary in a number of applications such as CO_2 injection in saline aquifers.

The chosen approach consisted in asymmetric modifications to the cubic EoS parameters as proposed by Søreide and Whitson: this allows an efficient and practical way to simulate hydrocarbon solubility in water and water vaporization within an existing simulator. Water phase density and viscosity computations were also adjusted to account for the effective aqueous phase composition.

The selected examples show that new GPU-based hardware is very well suited for running these compositional models. On the Smeaheia case, the overhead of two-components compositional runs was found to be about 60% over the corresponding black-oil model, inline with what reported by [9] for conventional simulations with two hydrocarbon components in equilibrium and dead water. This relatively modest cost means that compositional modeling can become a default, giving the engineers more flexibility in adding components as needed (e.g., to model depleted gas fields).

This work focused on supporting two-phase reservoir conditions. The next step will consist in developing and implementing a high-performance three-phase flash algorithm for GPUs, enabling full three-phase simulations. Use cases will include CO_2 enhanced oil recovery or CO_2 sequestration in retrograde condensate fields, as well as high-pressure/high-temperature gas fields where water vaporization can impact final recovery.

Acknowledgements The results presented in this paper have been achieved in the furtherance of a cooperative development agreement between Stone Ridge Technology and Eni S.p.A.

Data Availability Data supporting the findings of this study are available within the paper; data-sets are available from the corresponding author on reasonable request.

Declarations

Competing Interests The authors have no competing interests to declare that are relevant to the content of this article.

References

1. Afanasyev, A., Vedeneeva, E.: Compositional modeling of multicomponent gas injection into saline aquifers with the MUFITS simulator. J. Nat. Gas Sci. Eng. **94**, 103988 (2021)
2. Babaei, M.: Integrated carbon sequestration-geothermal heat recovery: performance comparison between open and close systems. Transp. Porous Media **126**(1), 249–273 (2019)
3. Bear, J.: Dynamics of fluids in porous media. Cour, Corp (1988)
4. Chabab, S., Theveneau, P., Coquelet, C., Corvisier, J., Paricaud, P.: Measurements and predictive models of high-pressure H2 solubility in brine (H2O+ NaCl) for underground hydrogen storage application. Int. J. Hydrog. Energy. **45**(56), 32206–32220 (2020)
5. Chang, Y.B., Coats, B., Nolen, J.: A compositional model for CO2 floods including CO2 solubility in water. SPE Reserv. Eval. Eng. **1**(02), 155–160 (1998)
6. Computer Modelling Group: GEM User Guide (2016)
7. Ennis-King, J., Paterson, L.: Role of Convective Mixing in the Long-Term Storage of Carbon Dioxide in Deep Saline Formations. SPE J. **10**(03), 349–356 (2005)
8. Equinor, Gassnova: Smeaheia on-line dataset. https://co2datashare.org/dataset/smeaheia-dataset (2022). Accessed 10 May 2022
9. Esler, K., Gandham, R., Patacchini, L., Garipov, T., Samardzic, A., Panfili, P., Caresani, F., Pizzolato, A., Cominelli, A.: A graphics processing unit-based, industrial grade compositional reservoir simulator. SPE J. **27**(01), 597–612 (2022)
10. Fawad, M., Mondol, N.H.: Geological and geophysical investigation of CO2 storage site Smeaheia in the northern North Sea. In: SEG Technical Program Expanded Abstracts 2019, Society of Exploration Geophysicists, pp. 3285–3289 (2019)
11. Gandham, R., Esler, K., Mukundakrishnan, K., Zhang, Y., Fang, C., Natoli, V.: GPU acceleration of equation of state calculations in compositional reservoir simulation. In: ECMOR XV-15th European Conference on the Mathematics of Oil Recovery. European Association of Geoscientists & Engineers, Amsterdam, The Netherlands (2016)
12. Gandham, R., Zhang, Y., Esler, K., Natoli, V.: Improving GPU throughput of reservoir simulations using NVIDIA MPS and MIG. In: Fifth EAGE Workshop on High Performance Computing for Upstream, 2021, 1–5 (2021)
13. Gassnova, G.: Feasibility study for full-scale CCS in Norway. Minist. Pet. Energy 1–62 (2016)
14. Gross, H., Mazuyer, A.: GEOSX: A multiphysics, multilevel simulator designed for exascale computing. SPE Reserv. Simul, Conf (2021)
15. Halliburton: Nexus Technical Reference Guide (2014)
16. Juanes, R., Spiteri, E., Orr Jr, F., Blunt, M.: Impact of relative permeability hysteresis on geological CO2 storage. Water Resour. Res. **42**(12) (2006)
17. Killough, J., Kossack, C.: Fifth comparative solution project: evaluation of miscible flood simulators. In: SPE Symposium on Reservoir Simulation. OnePetro (1987)
18. Korrani, A.K.N., Sepehrnoori, K., Delshad, M.: Coupling IPhreeqc with UTCHEM to model reactive flow and transport. Comput. Geosci. **82**, 152–169 (2015)
19. Kumar, A., Ozah, R., Noh, M., Pope, G.A., Bryant, S., Sepehrnoori, K., Lake, L.W.: Reservoir simulation of CO2 storage in deep saline aquifers. Spe J. **10**(03), 336–348 (2005)
20. Li, Y.K., Nghiem, L.X.: Phase equilibria of oil, gas and water/brine mixtures from a cubic equation of state and Henry's law. Can. J. Chem. Eng. **64**(3), 486–496 (1986)
21. Lorentz, J., Bray, B., Clark, C.: Calculating viscosity of reservoir fluids from their composition. J. Pet. Tech. **1171**, 231 (1964)
22. Michelsen, M., Mollerup, J.: Thermodynamic models: fundamentals and computational aspects. Tie-line Publications, Ronnebarvej, Denmark (2007)
23. Moortgat, J., Li, Z., Firoozabadi, A.: Three-phase compositional modeling of CO2 injection by higher-order finite element methods with CPA equation of state. In: SPE Reservoir Simulation Symposium. (2011)
24. Mukundakrishan, K., Rosa, A., Ranjan, S., Panfili, P., Cinquini, F., Cominelli, A., Patacchini, L., Esler, K.: Full-GPU simulation of coupled multi-reservoir models: implementation and field examples. In: SPE Reservoir Characterisation and Simulation Conference and Exhibition (2023)
25. Oldenburg, C.M.: Joule-Thomson cooling due to CO2 injection into natural gas reservoirs. Energy Convers. Manag. **48**(6), 1808–1815 (2007)
26. Open Porous Media: OPM Flow Reference Manual 2022-04 (2022)
27. Orsini, P., Ponting, D., Stone, D.: A study of temperature effects in the bunter closure 36, a potential large-scale CO2 Storage Site in UK. In: Proceedings of the 15th Greenhouse Gas Control Technologies Conference, pp. 15–18 (2021)
28. Pan, L., Spycher, N., Doughty, C., Pruess, K.: ECO2N V2. 0: A TOUGH2 fluid property module for mixtures of water, NaCl, and CO2. Scientific report LBNL-6930E (2015)
29. Pedersen, K., Fredenslund, A., Thomassen, P.: Properties of oils and natural gases, contributions in petroleum engineering. **5**, 199–207 (1989)
30. Peng, D.Y., Robinson, D.B.: A new two-constant equation of state. Ind. Eng. Chem. Fundam. **15**(1), 59–64 (1976)
31. Petitfrere, M., Patacchini, L., de Loubens, R.: Three-phase EoS-based reservoir simulation with salinity dependent phase-equilibrium calculations. In: ECMOR XV-15th European Conference on the Mathematics of Oil Recovery. European Association of Geoscientists & Engineers, cp–494 (2016)
32. Riaz, A., Hesse, M., Tchelepi, H., Orr, F.: Onset of convection in a gravitationally unstable diffusive boundary layer in porous media. J. Fluid Mech. **548**, 87–111 (2006)
33. Sandve, T., Rustad, A., Thune, A., Nazarian, B., Gasda, S., Rasmussen, A.: Simulators for the Gigaton Storage Challenge. A Benchmark Study on the Regional Smeaheia Model. In: EAGE GeoTech 2022 Sixth EAGE Workshop on CO2 Geological Storage, 2022. European Association of Geoscientists & Engineers, pp. 1–5 (2022)
34. Schlumberger: Eclipse 2019.1, Technical Description (2019a)
35. Schlumberger: Intersect 2019.1, Technical Description (2019b)
36. Soave, G.: Equilibrium constants from a modified Redlich-Kwong equation of state. Chem. Eng. Sci. **27**(6), 1197–1203 (1972)
37. Søreide, I., Whitson, C.H.: Peng-Robinson predictions for hydrocarbons, CO2, N2, and H2 S with pure water and NaCI brine. Fluid Phase Equilib. **77**, 217–240 (1992)
38. Vidyasagar, A., Patacchini, L., Panfili, P., Caresani, F., Cominelli, A., Gandham, R., Mukundakrishnan, K.: Full-gpu reservoir simulation delivers on its promise for giant carbonate fields. In: Third

EAGE WIPIC Workshop: Reservoir Management in Carbonates, 2019. European Association of Geoscientists & Engineers, pp. 1–5 (2019)
39. Wei, L.: Sequential coupling of geochemical reactions with reservoir simulations for waterflood and EOR studies. SPE J. **17**(02), 469–484 (2012)
40. Whitson, C.H., Brulé, M.R.: Phase behavior, 20. Society of Petroleum Engineers, Henry L. Doherty Memorial Fund of AIME (2000)
41. Yamamoto, H., Doughty, C.: Investigation of gridding effects for numerical simulations of CO2 geologic sequestration. Int. J. Greenh. Gas Control **5**(4), 975–985 (2011)
42. Yan, W., Huang, S., Stenby, E.H.: Measurement and modeling of CO2 solubility in NaCl brine and CO2-saturated NaCl brine density. Int. J. Greenh. Gas Control **5**(6), 1460–1477 (2011)
43. Yan, W., Michelsen, M.L., Stenby, E.H.: On application of non-cubic EoS to compositional reservoir simulation. In: SPE EUROPEC/EAGE Annual Conference and Exhibition. OnePetro (2011b)

Authors and Affiliations

P. Panfili[1] · L. Patacchini[2] · A. Ferrari[1] · T. Garipov[2] · K. Esler[2] · A. Cominelli[1]

L. Patacchini
lpatacchini@stoneridgetechnology.com

A. Ferrari
andrea.ferrari2@eni.com

T. Garipov
tgaripov@stoneridgetechnology.com

K. Esler
kesler@stoneridgetechnology.com

A. Cominelli
acominelli@eni.com

[1] Eni S.p.A., via Emilia 1, 20097 San Donato Milanese, MI, Italy

[2] Stone Ridge Technology, 2015 Emmorton Rd, Bel Air, MD 21015, USA